Catalysis Science & Technology

ROYAL SOCIETY OF CHEMISTRY

PAPER

View Article Online
View Journal | View Issue

Cite this: *Catal. Sci. Technol.*, 2022, 12, 250

Revealing long-lived electron–hole migration in core–shell α/γ-Fe_2O_3/FCP for efficient photoelectrochemical water oxidation†

Yinyin Li,[a] Yifan Chen,[b] Qiannan Wu,[c] Rui Zhang,[a] Mingjie Li,[b] Yanhong Lin,[a] Dejun Wang[a] and Tengfeng Xie *[a]

The oxygen evolution reaction (OER) of Fe_2O_3 is limited by its low photocarrier separation efficiency in photoelectrochemical (PEC) water splitting. How to construct an effective photocarrier transmission route in Fe_2O_3 has become an important bottleneck for enhancing OER performance. Herein, we exploit a core–shell nanorod structure loaded with FeCo Prussian blue (FCP) to boost the water oxidation kinetics and charge transfer efficiency for the first time. As expected, the optimal γ-Fe_2O_3/α-Fe_2O_3 photoanode exhibits a remarkable photocurrent density of 2.4 mA cm^{-2} at 1.23 V *vs.* RHE; when a cocatalyst FCP is introduced as a hole-transport layer, it shows a photocurrent density of 3.5 mA cm^{-2} at 1.23 V *vs.* RHE, which is 8.7 times higher than that of the pure α-Fe_2O_3. The outstanding photochemical performance could be attributed to the highest separation efficiency. A further study on the carrier lifetime was performed and clarified that the photocarrier lifetime of the γ-Fe_2O_3/α-Fe_2O_3/FCP photoanode is prolonged (~50.64 ps) as compared to that of the pure α-Fe_2O_3 photoanode (~21.00 ps) using femtosecond time-resolved absorption spectroscopy (fs-TAS). This work successfully explains the photocatalytic water oxidation mechanism in the γ-Fe_2O_3/α-Fe_2O_3/FCP photoanode and provides an effective insight into designing a photocarrier delivery channel for the outstanding water oxidation.

Received 7th September 2021,
Accepted 2nd November 2021

DOI: 10.1039/d1cy01628h

rsc.li/catalysis

1. Introduction

Photoelectrochemical (PEC) water splitting is regarded as the promising strategy to solve the energy crisis.[1–3] However, the rate of the photoanode reaction is lower than that of the water reduction reaction.[4,5] Therefore, improving the efficiency of the water oxidation reaction is the key to optimize the process of water splitting. In particular, α-Fe_2O_3 is an excellent candidate for sunlight-driven PEC water oxidation with good sunlight harvesting capability, outstanding stability and nontoxic nature.[6–8] Theoretically, hematite possesses a high solar-to-hydrogen efficiency (16.8%) and a maximum photocurrent of 12.6 mA cm^{-2}.[9–11] However, the strong recombination of photo-generated carriers and the short hole-diffusion length of pure α-Fe_2O_3 make it have poor water oxidation ability to meet practical applications. Therefore, various remarkable strategies have been progressed to achieve effective water oxidation kinetics and charge separation and these involve ion doping (Ti^{4+}, Ta^{4+}, Sn^{4+}, *etc.*),[12–15] heterojunctions,[16–18] morphology control, oxygen vacancies,[19] and oxygen-evolution cocatalysts (InOOH, Fh, and CoPi).[20–23]

Among these strategies, constructing heterojunctions is able to make use of the interfacial electric field for further enhancing spatial charge separation, such as Co_3O_4/Ti–Fe_2O_3,[24] Fe_2O_3/CdS,[25,26] Fe_2O_3/g-C_3N_4,[27] and V_2O_5/ZnO.[28] However, the interfacial charge transfer in heterojunctions is hindered due to the presence of lattice matching with different degrees between different semiconductors. As an alternative, formation of phase junctions with the same composition was found to be an effective strategy to improve efficient charge separation. Accordingly, like WO_3,[29] TiO_2[30] and poly(1,4-diethynylbenzene)[31] have been successfully fabricated and showed excellent charge separation efficiency. Moreover, few research studies provided an in-depth explanation on the dynamic electron and hole transfer processes using fs-TAS. Therefore, fs-TAS is necessary to study the role of phase junctions and cocatalysts in the photocatalytic OER process.

In this work, a Ti^{4+}-doped phase junction with a hydrophilic ultrathin FeCo Prussian blue (FCP) photoanode was synthesized *via* a simple hydrothermal method.[10,32] As

[a] *Institute of Physical Chemistry, College of Chemistry, Jilin University, Changchun 130012, P. R. China. E-mail: xietf@jlu.edu.cn*
[b] *Department of Applied Physics, The Hong Kong Polytechnic University, Hung Hom, Kowloon, Hong Kong*
[c] *State Key Laboratory of Inorganic Synthesis and Preparative Chemistry, College of Chemistry, Jilin University, Changchun 130012, P. R. China*

† Electronic supplementary information (ESI) available. See DOI: 10.1039/d1cy01628h

expected, the optimal γ-Fe_2O_3/α-Fe_2O_3/FCP photoanode exhibits a photocurrent density of 3.5 mA cm^{-2} at 1.23 V *vs.* RHE, which is 8.7 times higher than that of pure α-Fe_2O_3. More importantly, the fs-TAS results demonstrate that the excellent synergies between the phase junction and FCP could not only facilitate the photoexcited hole transfer, but also maintain long-lived charge separation states (~50.64 ps). This work provides distinct insights into designing excellent catalysts in water oxidation.

2. Experimental section

2.1 Materials

Ferric chloride hexahydrate ($FeCl_3 \cdot 6H_2O$; 97.0–102%) was bought from Alfa Aesar. Potassium ferricyanide ($K_3[Fe(CN)_6]$), titanium tetrachloride ($TiCl_4$) and sodium nitrate ($NaNO_3$) were purchased from Sinopharm Reagent. Cobalt chloride ($CoCl_2$) and cobalt nitrate hexahydrate ($Co(NO_3)_2 \cdot 6H_2O$) were bought from Shanghai Reagent. All materials were used without further purification.

2.2 Synthesis of the Ti–Fe_2O_3 bottom layer

According to the previous report, Ti–Fe_2O_3 nanorod arrays could be successfully hydrothermally prepared on FTO substrates.[33] The FTO glass was ultrasonically cleaned with acetone and ethanol to make its surface clean. To obtain the hydrothermal precursor solution, 0.5063 g $FeCl_3 \cdot 6H_2O$ and 1.0625 g $NaNO_3$ were mixed in deionized water (100 mL) under stirring for 20 min. Subsequently, different volume amounts of $TiCl_4$ solution (75 μL, 175 μL, and 275 μL) were added to the precursor solution. Then, the mixed aqueous solutions with different doping volumes of $TiCl_4$ solution were transferred into a 50 mL Teflon-lined autoclave inserted with FTO, and then heated to 100 °C for 12 h in an oven. After the oven was cooled down to room temperature, the obtained Ti–FeOOH was taken out and annealed at 550 °C for two hours under an air atmosphere. On the basis of different Ti doping volumes, the samples were denoted as 75Fe_2O_3 (75 μL), 175Fe_2O_3 (175 μL) and 275Fe_2O_3 (275 μL). The main reactions are listed as follows:[34]

$$Fe^{3+} + 2H_2O = FeOOH + 3H^+$$

$$2FeOOH = \alpha\text{-}Fe_2O_3 + H_2O$$

2.3 Synthesis of the γ-Fe_2O_3/α-Fe_2O_3 phase junction

2.025 g $FeCl_3 \cdot 6H_2O$ and 4.25 g $NaNO_3$ were dissolved in deionized water, and the $TiCl_4$ ethanol solution (75 μL) was mixed with the above solution (100 mL) to form a hydrothermal precursor solution. Then, a piece of the Ti–Fe_2O_3 bottom layer was placed into the autoclave with its conducting side facing down. The autoclave was maintained at 100 °C for 12 h and allowed to cool naturally. Subsequently, the obtained samples were washed by water several times and annealed at 550 °C for 2 h. Interestingly, several nano-sized γ-Fe_2O_3 formed during the second calcination process, and the conversion mechanism was evaluated using the equations below:[35]

$$\alpha\text{-}Fe_2O_3 + 6H^+ \rightarrow 2Fe^{3+} + 3H_2O$$

$$2Fe^{3+} + 6NO_3^- \rightarrow 2\gamma\text{-}Fe_2O_3 + 6NO_x$$

$$Fe^{3+} + 2H_2O \rightarrow FeOOH + 3H^+$$

$$\gamma\text{-}Fe_2O_3/FeOOH \rightarrow \gamma\text{-}Fe_2O_3/\alpha\text{-}Fe_2O_3 + H_2O$$

Therefore, after the second hydrothermal treatment and calcination, the core–shell γ-Fe_2O_3/α-Fe_2O_3 was successfully formed. In addition, according to the different Ti doping volumes, the composite samples were denoted as 75Ti–Fe_2O_3/75Ti–Fe_2O_3, 175Ti–Fe_2O_3/75Ti–Fe_2O_3 and 275Ti–Fe_2O_3/75Ti–Fe_2O_3. It was worth noting that in the following description, we denoted 175Ti–Fe_2O_3/75Ti–Fe_2O_3 as γ-Fe_2O_3/α-Fe_2O_3.

2.4 Synthesis of the γ-Fe_2O_3/α-Fe_2O_3/FCP photoanode

The amorphous FeCo Prussian blue (FCP) cocatalyst was loaded by sequentially dipping the γ-Fe_2O_3/α-Fe_2O_3 phase junction in 0.02 M $K_3[Fe(CN)_6]$ aqueous solution and 0.04 M $CoCl_2$ aqueous solution through a method described previously.[36] First, the phase junction was immersed in $K_3[Fe(CN)_6]^{3-}$ solution for 15 min and $CoCl_2$ solution for another 15 min, alternately, followed by rinsing with deionized water and drying in air. It is necessary to repeat this step several times (two to five) to obtain the optimized photoanode. Furthermore, the obtained samples are heated at 25, 75 and 300 °C to generate the best performance.

2.5 Synthesis of the γ-Fe_2O_3/α-Fe_2O_3/Co-Pi photoanode

A representative three-electrode system was used for the electrodeposition of cobalt phosphate (CoPi) on γ-Fe_2O_3/α-Fe_2O_3.[22] Herein, this electrodeposition process was carried out at a constant potential of 1 V (*vs.* Ag/AgCl), in which the obtained γ-Fe_2O_3/α-Fe_2O_3 substrate served as the working electrode, a Pt sheet as the counter electrode, and Ag/AgCl as the reference electrode. In addition, the electrolyte was prepared by dissolving 0.1 M potassium phosphate and 0.5 mM $Co(NO_3)_2 \cdot 6H_2O$ in water (pH = 7). In this work, the electrodeposition time was 200 s to obtain the photoanode.

2.6 Structural characterization

X-ray diffraction with Cu Kα radiation (XRD, D/MAX2250 diffractometer) was applied to analyse the crystal structure from 10° to 80° at a scan rate of 10° min^{-1}. Field-emission

scanning electron microscopy (SEM; Hitachi Company) was conducted to examine the surface morphology and film thickness. High-resolution transmission electron microscopy (HR-TEM; FEI Tecnai G2 F20) and the related energy-dispersive X-ray spectrometry (EDX) were used to further analyse the elemental composition. X-ray photoelectron spectroscopy (XPS) was performed to explore the surface chemical state of elements by using the C 1s peak as a correction. A UV-vis-NIR spectrophotometer (Shimadzu UV-3600) recorded the UV-vis absorption spectrum of the samples with $BaSO_4$ as the reference. The lock-in-based SPV measurements and TPV measurements on home-made equipment were applied to measure the separation and kinetic behaviours of photogenerated charge carriers.

A Helios pump/probe setup (Ultrafast Systems LLC) could be used to perform transient absorption (TA) spectroscopy. 800 nm fs laser pulses were generated from the amplifier (Coherent Libra, 50 fs, 1 kHz). Besides, we use a 3 mm sapphire crystal to product the white light continuum probe, and use a BBO crystal with frequency doubling the 800 nm to produce 400 nm pump pulses. In addition, the diameter of the pump beam spot is 2 mm, the pump power is 30 μW, and probe beam is 50 μm. The probe beam passing through the sample was collected using a UV-vis detector (CCD sensor).

2.7 PEC measurements

The PEC measurements of the composite phase junction were evaluated in a standard three-electrode system. The working electrode, counter electrode and reference electrode are the as-synthesized phase junction, the Pt sheet, and Ag/AgCl, respectively, which make up the CHI 660E electrochemical workstation. The illuminated area was controlled to 0.283 cm^2, and 1 M KOH aqueous solution (pH = 13.6) was applied as the electrolyte. A 300 W xenon lamp (Microsolar 300, Beijing Perfect light) was used to simulate AM 1.5 G illumination (100 mW cm^{-2}).

The applied potential *versus* Ag/AgCl was translated into potential *versus* RHE based on the Nernst equation:

$$E_{RHE} = E_{Ag/AgCl} + 0.059\ \text{pH} + E^{\theta}_{Ag/AgCl}$$

The electrolyte in our PEC measurements was 1 M KOH (pH = 13.6) unless otherwise specified, and the active area was 0.283 cm^2. The current *vs.* potential curve was obtained by linear sweep voltammetry (LSV) at a scan rate of 10 mV s^{-1}.

Applied bias photon to current efficiency (ABPE) was calculated *via* the following equation:

$$\text{ABPE} = \left(J_{light} - J_{dark}\right) \times \left(\frac{1.23 - V_{RHE}}{P_{light}}\right)$$

where J_{light} and J_{dark} referred to the current densities of the synthesized photoanodes under illumination and in the dark, respectively. V_{RHE} referred to the applied potential *versus* RHE, and P_{light} referred to the incident light intensity (100 mW cm^{-2}).

The injection efficiency of the photoanodes was obtained through employing 0.5 M H_2O_2 as a hole scavenger in the 1 M KOH electrolyte, and the oxidation of H_2O_2 is thermodynamically and kinetically more favorable than that of water. The injection efficiency (η_{inj}) was determined by using the following equation:

$$\eta_{inj} = J_{H_2O}/J_{H_2O_2}$$

where J_{H_2O} and $J_{H_2O_2}$ referred to the photocurrent density for PEC H_2O oxidation and PEC H_2O_2 oxidation, respectively.

The separation efficiency of photogenerated charge carriers during the reaction was characterized by the difference values of open circuit potential between the dark and illumination conditions.

Electrochemical impedance spectroscopy (EIS) was conducted with a frequency range of 10^5 Hz–0.05 Hz at 1.0 V *vs.* RHE under illumination (100 mW cm^{-2}) to ascertain the charge transport of the photoanode. The EIS spectrum was fitted using the ZView software according to the following fitted model:

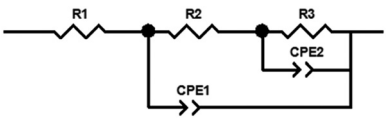

The incident photon to current conversion efficiency (IPCE) was measured at 1.23 V *vs.* RHE with the help of a monochromator, and the intensity of monochromatic light was measured using a calibrated Si photodiode. The IPCE was obtained according to the equation:

$$\text{IPCE} = \frac{J \times 1240}{P_{mono} \times \lambda}$$

Mott–Schottky analysis: in the M–S plot, the flat band potential of the photoelectrode is measured according to following equation:

$$\frac{1}{C^2} = \frac{2}{e\varepsilon\varepsilon_0 N_D}\left[(E - E_{FB}) - \frac{\kappa T}{e}\right]$$

in which C is the space charge capacitance, e is the electron charge, ε is the vacuum permittivity (8.85 × 10^{-12} F m^{-1}), ε_0 is the relative dielectric constant of hematite (ε_0 = 80), N_D is the charge donor density (cm^{-3}), E is the electrode applied potential, E_{FB} is the flat band potential, κ is the Boltzmann constant (1.38 × 10^{-23} J K^{-1}) and T is the absolute temperature (in K).

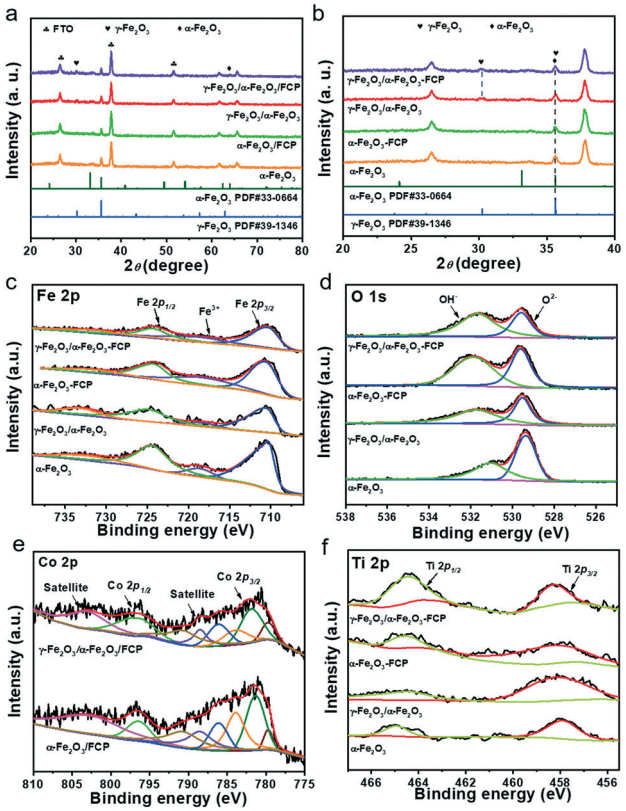

Fig. 1 (a) XRD patterns of the α-Fe_2O_3-based photoanodes; (b) enlarged XRD patterns in the range of 20–40°. XPS spectra of the α-Fe_2O_3-based photoanodes: Fe 2p (c); O 1s (d); Co 2p (e); Ti 2p (f).

3. Results and discussion

3.1 Composition and chemical state

X-ray diffraction (XRD) patterns could be measured to examine the crystalline structure of the samples (Fig. 1a). After the first hydrothermal treatment, the typical diffraction peaks located at 35.6° and 64° are indexed to the pure α-Fe_2O_3 (JCPDS No. 33-0664).[37] After the second hydrothermal reaction, besides the characteristic peaks of α-Fe_2O_3, a new characteristic peak of 31.2° could be found from the enlarged XRD pattern as shown in Fig. 1b, which could be attributed to the characteristic peak of γ-Fe_2O_3 (JCPDS No. 39-1346).[38] To further confirm the crystalline structure of γ-Fe_2O_3, the XRD pattern of the sample powder fabricated by the same method was obtained. The powder XRD patterns of γ-Fe_2O_3/α-Fe_2O_3 were obtained as shown in Fig. S1,† and the major diffraction peaks at 35.5° (311), 43.5° (400), 57.5° (511), and 63° (440) are in good agreement with γ-Fe_2O_3 (JCPDS No. 39-1346). Nevertheless, there is no evident diffraction peaks corresponding to the FeCo Prussian blue (FCP), which may result from its amorphous structure and ultrathin thickness. In order to further study the chemical states, X-ray photoelectron spectroscopy (XPS) is carried out. Fig. 1c reveals that there are two characteristic peaks at 710.5 eV and 724.1 eV, which correspond to Fe $2p_{3/2}$ and Fe $2p_{1/2}$. For pure α-Fe_2O_3, four characteristic peaks (709.9, 710.7, 711.5 and 713.4 eV) of Fe $2p_{3/2}$ could be fitted, while two new characteristic peaks (713.1 and 711.4 eV) belonging to γ-Fe_2O_3 are present. After loading FCP on the γ-Fe_2O_3/α-Fe_2O_3 sample, another peak (714.2 eV) could be assigned to an Fe–Co bond that emerged.[22,39–41] In Fig. 1d, the spectrum of the O 1s region exhibits two peaks (531.6 and 529.5 eV) corresponding to the lattice oxygen (OH^-) and hydroxyl oxygen (O^{2-}).[42] Moreover, the peaks located at 796.7 and the six characteristic peaks (779.9, 782.0, 783.8, 786.2, 788.4 and 790.7 eV) of γ-Fe_2O_3/α-Fe_2O_3/FCP and γ-Fe_2O_3/α-Fe_2O_3 are found to be the splitting signals of Co $2p_{1/2}$ and Co $2p_{3/2}$ (Fig. 1e), respectively.[43] As illustrated in Fig. 1f, two peaks located at 464.3 eV (Ti $2p_{1/2}$) and 458.3 eV (Ti $2p_{3/2}$) for Ti 2p are observed, which can correspond to Ti^{4+}.[44] In addition, the survey scan spectrum of the γ-Fe_2O_3/α-Fe_2O_3/FCP and γ-Fe_2O_3/α-Fe_2O_3 photoanodes is shown in Fig. S2,† revealing that Fe, O, Co, and Ti are all detected. Moreover, the Raman spectra of γ-Fe_2O_3/α-Fe_2O_3 and α-Fe_2O_3 were measured as shown in Fig. S3,† and this also confirms the existence of γ-Fe_2O_3.

Fig. 2a shows the schematic of the overall hydrothermal procedure of the core–shell structure. To study the morphologies of the as-prepared samples, the top-view and cross-sectional images from scanning electron microscopy (SEM) are shown in Fig. 2b and c; herein, the γ-Fe_2O_3/α-

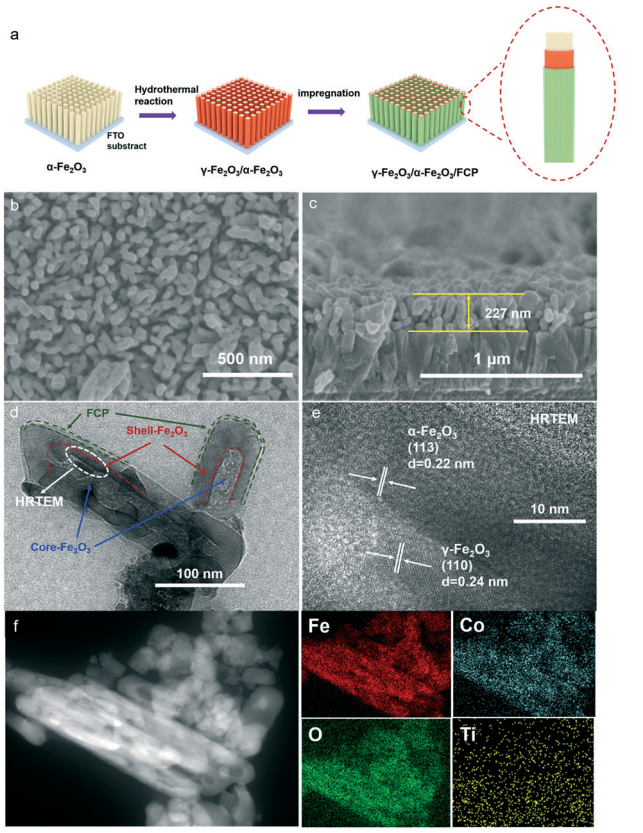

Fig. 2 (a) Fabrication diagram of the nanoarrays. (b) Superficial SEM image of γ-Fe_2O_3/α-Fe_2O_3/FCP. (c) Cross-sectional image of γ-Fe_2O_3/α-Fe_2O_3/FCP. (d) Magnified image of the core–shell structure of γ-Fe_2O_3/α-Fe_2O_3/FCP. (e) HR-TEM image of γ-Fe_2O_3/α-Fe_2O_3/FCP. (f) EDX elemental mapping of γ-Fe_2O_3/α-Fe_2O_3/FCP.

Fe_2O_3/FCP sample is made up of uniform and homogeneous nanorod arrays. There is no change in the surface morphology between γ-Fe_2O_3/α-Fe_2O_3 and the pristine α-Fe_2O_3 (Fig. S4).† Moreover, the high-resolution transmission electron microscopy (HR-TEM) image clearly reveals that the obtained photoanodes possess a core–shell structure, and the amorphous FCP was simultaneously formed on their surfaces (Fig. 2d). The typical lattice fringes of the phase junction (0.24 nm) belong to the (110) plane of γ-Fe_2O_3, while another lattice fringe (0.22 nm) could correspond to the (113) plane of α-Fe_2O_3 (Fig. 2e).[45] In addition, the Fe, O, Co and Ti elements in γ-Fe_2O_3/α-Fe_2O_3/FCP demonstrate that the FCP nanoparticles were uniformly dispersed in the γ-Fe_2O_3/α-Fe_2O_3 sample (Fig. 2f).

3.2 The synergistic effect of the phase junction and FCP in PEC water-oxidation performance

The PEC measurement is a basic strategy to systematically investigate the performance of the photoanode with the solar simulated light illumination (AM 1.5 G, 100 mW cm^{-2}). Firstly, to verify the photocatalysis potential, the photoanodes are optimized by adjusting different Ti-doping volumes in the Fe_2O_3 bottom layer. As shown in Fig. S5a,† the core–shell phase junction with the 175 μL doping volume of Ti^{4+} in the Fe_2O_3 bottom layer possesses the best photocurrent response (denoted as γ-Fe_2O_3/α-Fe_2O_3). In addition, the ABPE and IPCE measurements (Fig. S5b and c†) also indicate that this phase junction exhibits the highest IPCE value (58% at 390 nm) and ABPE value (0.169%). Particularly, when modifying with the ultrathin FCP layer (Fig. 3a), the γ-Fe_2O_3/α-Fe_2O_3/FCP sample achieves excellent PEC performance; it is worth noting that the reaction time and temperature of FCP were optimized to obtain the optimal sample (Fig. S6);† the optimized current could reach 3.5 mA cm^{-2} at 1.23 V *vs.* RHE, which is 8.5 times greater than that of pure α-Fe_2O_3. And the sample exhibits a ~90 mV cathodic shift of the onset potential (Fig. S7†). In addition, FCP has a better photocatalytic performance than cobalt phosphate (CoPi) (Fig. S8†). The above analysis implies that the synergistic effect of the phase junction and FCP could optimize the performance in water oxidation. In order to comprehensively understand the role of the phase junction and FCP in improving the PEC performance, transient photocurrent response measurements under chopped light with a frequency of 0.25 Hz are employed (Fig. 3b). It shows that the photocurrent densities follow the trend γ-Fe_2O_3/α-Fe_2O_3/FCP > γ-Fe_2O_3/α-Fe_2O_3 > α-Fe_2O_3/FCP > α-Fe_2O_3, suggesting that the surface decoration of FCP and γ-Fe_2O_3 is unable to improve the water oxidation capacity. Further, chronoamperometric measurements based on *i*–*t* curves at 1.23 V *vs.* RHE are also performed (Fig. 3c), which is also consistent with the LSV results. Meanwhile, γ-Fe_2O_3/α-Fe_2O_3/FCP shows the highest ABPE as compared to others, and its value could reach up to 0.38% at 1.02 V_{RHE} (Fig. 3d). And the γ-Fe_2O_3/α-Fe_2O_3/FCP sample exhibits the highest IPCE value of 87% at 390 nm (Fig. 3e). Moreover, after 2 h photostability measurements, the γ-Fe_2O_3/α-Fe_2O_3/FCP and γ-Fe_2O_3/α-Fe_2O_3 samples could maintain about 94% and 97% of the initial photocurrent density (Fig. 3f), respectively. Interestingly, the contact angle of γ-Fe_2O_3/α-Fe_2O_3/FCP and α-Fe_2O_3 (Fig. 3f) was also measured to elucidate the liquid surface adhesion. Herein, a relatively smaller contact angle is obtained for γ-Fe_2O_3/α-Fe_2O_3/FCP, indicating that γ-Fe_2O_3/α-Fe_2O_3/FCP possesses the outstanding hydrophilic properties in the observed excellent PEC performance.

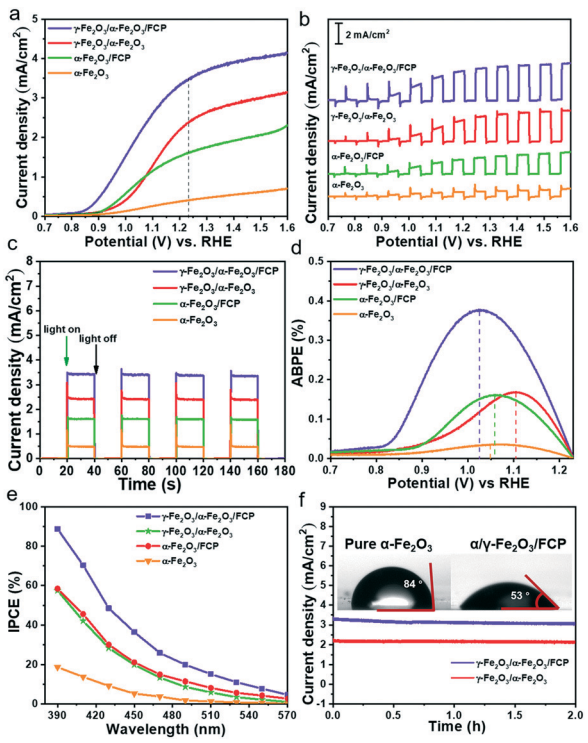

Fig. 3 (a) Current density–potential curves. (b) LSV curves under chopped light. (c) *i*–*t* curves at 1.23 V_{RHE}. (d) ABPE spectra. (e) IPCE plots at 1.23 V *vs.* RHE. (f) Results of the PEC OER stability test at 1.23 V *vs.* RHE in KOH electrolyte. The inset shows the water contact angle under ambient conditions.

Typically, three key factors in developing suitable photocatalysts could be attributed to solar light harvesting, photocarrier separation and injection efficiency.[46,47] First, the UV-vis diffuse reflectance spectra of the photoanode are measured (Fig. S9a),† and the light absorption wavelength edge of all the samples is around 600 nm. The bandgaps (E_g) of α-Fe_2O_3 could be estimated to be 2.11 eV based on the corresponding Tauc analysis (Fig. S9b).† These results indicate that both phase junction and FCP have no significant effect on the absorption properties. Consequently, it is reasonable to deduce that the enhanced charge separation and injection efficiency are the main reasons for the enhanced PEC performance.

Based on the above analysis and assumptions, open-circuit photovoltage (OCP) measurements are carried out to verify the effects on the behaviour of generated charges (Fig. 4a). In this work, the open circuit voltage (OCP) is the

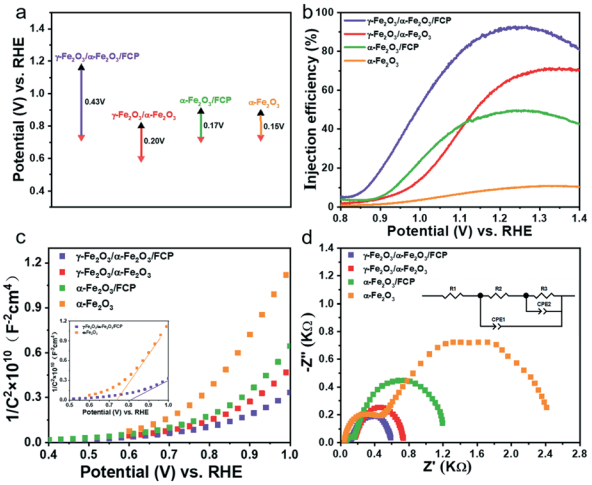

Fig. 4 (a) Open circuit potentials (OCPs) in 1 M KOH electrolyte. (b) Injection efficiencies. (c) M–S plots. The inset shows the enlarged Mott–Schottky curves. (d) Nyquist plots at 1.0 V *vs.* RHE.

difference value between the open circuit voltage in the dark state (V_{dark}) and the open circuit voltage under the light state (V_{light}). The open circuit voltages in the dark state and the light state used here are both stable voltage values. The γ-Fe_2O_3/α-Fe_2O_3/FCP sample exhibits the highest OCP values, suggesting that the composite photoanode could offer an additional intrinsic built-in electric field to boost the driving force of charge separation. Besides, the injection efficiency of the photoanodes in 1 M KOH with or without 0.5 M H_2O_2 could be used to estimate the charge transfer efficiency at the interface between the phase junction and FCP (Fig. 4b). The hole injection efficiency is significantly improved when the phase junction and FCP are introduced. Meanwhile, M–S plot analysis is conducted to obtain underlying information about the charge transfer process, in which a much flatter slope for γ-Fe_2O_3/α-Fe_2O_3/FCP could be achieved as shown in Fig. 4c. Particularly, the N_D values of α-Fe_2O_3 and γ-Fe_2O_3/α-Fe_2O_3/FCP are 4×10^{19} cm^{-3} and 1.15×10^{20} cm^{-3}, respectively (see the inset in Fig. 4c). This result implies a substantially higher charge carrier density, which leads to the effective charge separation and transfer. Moreover, we investigate the driving force at the interfacial electric field between α-Fe_2O_3 and the FCP through the WF measurements (Fig. S10),† which directly reveals the contact potential difference (CPD) between the sample and the Au probe. The WF values are calculated based on the following equation:

$$\Phi_{sample} = \Phi_{Au} + eCPD \ (\Phi_{Au} = 4.8 \text{ eV})$$

Herein, the WF values of α-Fe_2O_3 and the FCP were determined to be 4.71 and 5.07 eV, respectively. The results indicated that the Fermi level of α-Fe_2O_3 is higher than that of FCP, and the free electrons would transfer from α-Fe_2O_3 to FCP until the Fermi level is aligned when FCP is deposited on α-Fe_2O_3. It has been clearly demonstrated earlier that the interfacial electric field is oriented from α-Fe_2O_3 to FCP, which could facilitate the hole transfer from α-Fe_2O_3 to FCP.

To further illustrate the impressive role of the phase junction and FCP in the charge transfer process, electrochemical impedance spectroscopy (EIS) analysis was conducted. It should be noted that the small and the large semicircle are relative to the charge transfer resistance (R_2) at the solid/solid interface and the charge injection resistance (R_3) at the photoanode/electrolyte interface, respectively.[48,49] As shown in Fig. 4d, the typical EIS Nyquist plots of the obtained four photoanodes are fitted using the equivalent circuit model. Their results are listed in Table S1† and the equivalent circuit is shown in Fig. S11.† It is worth mentioning that the charge transfer resistance (R_2) at the interface of γ-Fe_2O_3 and α-Fe_2O_3 dramatically lowered, which suggests that the phase junction is expected to accelerate the charge separation. It is apparent that a drastically decreased radius of γ-Fe_2O_3/α-Fe_2O_3/FCP is found relative to γ-Fe_2O_3/α-Fe_2O_3, which means that the R_3 of photogenerated holes is dramatically reduced due to the superior catalytic properties of FCP.

3.3 The charge carrier dynamics of the α-Fe_2O_3-based photoanodes

To deeply understand the transfer and separation of photogenerated charges, a surface/transient photovoltage (SPV/TPV) test is conducted (introduction of instruments in the ESI†). Theoretically, the SPV signal could be used to deduce the separation efficiency of the photocatalyst. And the stronger signal indicates better separation efficiency.[50–53] As shown in Fig. 5a, pure α-Fe_2O_3 exhibits a relatively weak SPV signal while γ-Fe_2O_3/α-Fe_2O_3/FCP shows the strongest SPV values. Besides, the conventional TPV signal of the phase junctions under 532 nm laser pulse is implemented to

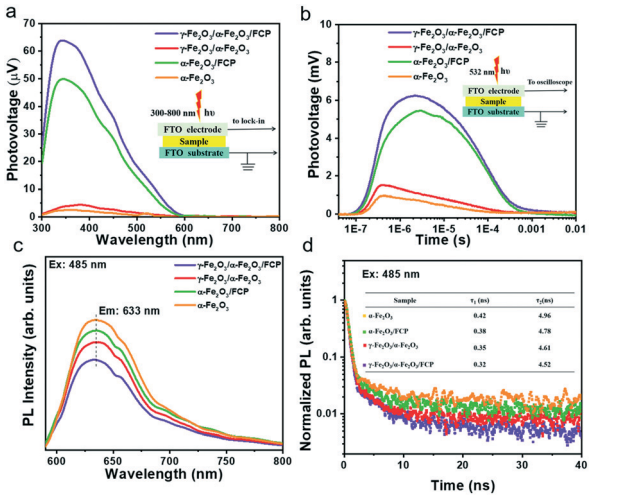

Fig. 5 (a) SPV signal. The inset shows the schematic of the SPV measurements. (b) TPV signal from front side illumination. The inset shows the schematic of the TPV measurements. (c) Steady-state photoluminescence (PL) spectra at the excitation wavelength of 485 nm produced by a xenon lamp. (d) Results of time-resolved photoluminescence (TRPL) excited by a 485 nm pumped pulsed laser.

confirm the transfer processes of photogenerated charge carriers. The increasing signal suggests the outstanding separation efficiency. As shown in Fig. 5b, the γ-Fe_2O_3/α-Fe_2O_3/FCP photoanode prolongs the lifetime of photogenerated charges and effectively suppresses charge recombination. Moreover, we employed photoluminescence (PL) spectroscopy to further explore the charge recombination behaviors. The peaks at 633 nm (Fig. 5c) indicated that the synergistic effect of FCP and the core–shell phase junction was effective in suppressing the charge recombination. In addition, time-resolved photoluminescence (TRPL) was conducted to further understand the role of FCP and the phase junction in the dynamics of charge carriers. And the PL decay spectrum (Fig. 5d) was fitted using the biexponential function for obtaining the first fast decay and the later slow decay (inset in Fig. 5d). Herein, the fast lifetime (τ_1) of the samples decreased from 0.42 to 0.32 ns when γ-Fe_2O_3/α-Fe_2O_3/FCP was formed, and the slow lifetime (τ_2) of the γ-Fe_2O_3/α-Fe_2O_3/FCP photoanode drastically reduced from 4.96 to 4.52 ns; double-exponential fitting is suitable for the PL decay curve probed at 485 nm (Fig. S12).† These results fully explained that the introduction of FCP and the phase junction could effectively improve the charge separation efficiency.

Femtosecond time-resolved transient absorption spectroscopy (fs-TAS) is applied to investigate the electron–hole separation efficiency and understand the kinetics process of oxygen production on the PEC performance. Herein, fs-TAS is used to track the real-time photogenerated hole dynamics under 400 nm excitation.[13,54–57] All samples obtained a broad negative absorption band as shown in Fig. 6a–d, due to the presence of the state filling of photobleaching and the stimulated emission. Compared with pure α-Fe_2O_3, the more intensive negative signal of γ-Fe_2O_3/α-Fe_2O_3 suggests that more photogenerated holes in the phase junction could be extracted from bulk. Moreover, the further improvement of the signal is mainly due to the ultrathin catalyst FCP; it is obvious that the FCP has a positive effect on the PEC performance. In addition, as shown in Fig. 6e–i, double-exponential fitting is suitable for the TAS decay curve probed at 585 nm in order to study the decay kinetics of photo-generated holes, and the related parameters are shown in Table S2.† Theoretically, the short lifetime (τ_1) and long lifetime (τ_2) components could be used to estimate the recombination degree. The prolonged lifetimes of the γ-Fe_2O_3/α-Fe_2O_3 and γ-Fe_2O_3/α-Fe_2O_3/FCP photoanodes are largely increased (τ_1: 0.94 ± 0.014 ps; τ_2: 33.45 ± 0.50 ps and τ_1: 1.31 ± 0.029 ps; τ_2: 50.64 ± 0.78 ps, respectively), as compared to that of pure α-Fe_2O_3 (τ_1: 0.81 ± 0.019 ps; τ_2: 21.00 ± 0.58 ps). As we know, during the PEC water splitting reaction, more longer-lived photogenerated holes on the surface are more beneficial for the PEC water splitting reaction, and the lifetimes of the different photoanodes follow the order γ-Fe_2O_3/α-Fe_2O_3/FCP > γ-Fe_2O_3/α-Fe_2O_3 > α-Fe_2O_3/FCP > α-Fe_2O_3, which is consistent with the results of the PEC performance. In addition, the pseudocolor TA plots (Fig. S13†) of the α-Fe_2O_3-based photoanodes indicate that the active ultralong lived charge separation state facilitates the water oxidation.

According to the above conclusion, Scheme 1 shows the schematic band diagram of the γ-Fe_2O_3/α-Fe_2O_3/FCP composite photoanode for water oxidation. In this system, benefitting from the enhanced charge separation, the holes of γ-Fe_2O_3 could timely transfer to α-Fe_2O_3 at the γ-Fe_2O_3/α-Fe_2O_3 interface. Meanwhile, the holes on α-Fe_2O_3 quickly captured by FCP could further participate in the water splitting reaction.

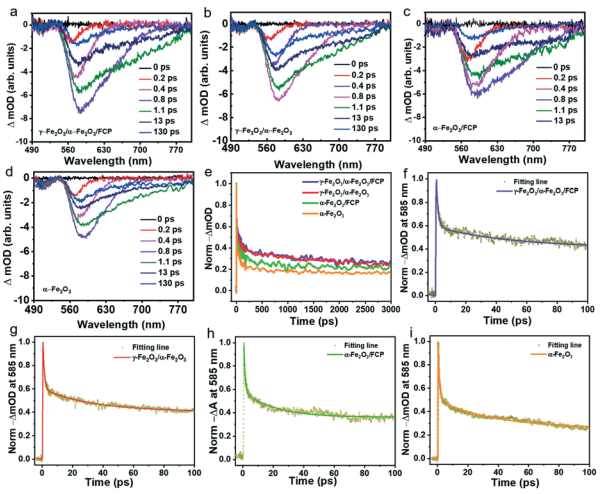

Fig. 6 TAS spectra of a) γ-Fe_2O_3/α-Fe_2O_3/FCP, b) γ-Fe_2O_3/α-Fe_2O_3, c) α-Fe_2O_3/FCP, and d) α-Fe_2O_3 pumped by a 400 nm femtosecond laser. e) Time profiles of the normalized TAS at 585 nm. Experimental decay kinetics fitted at 585 nm: f) γ-Fe_2O_3/α-Fe_2O_3/FCP, g) γ-Fe_2O_3/α-Fe_2O_3, h) α-Fe_2O_3/FCP and i) α-Fe_2O_3.

4. Conclusions

In this study, it is demonstrated that both phase junction and FCP in γ-Fe_2O_3/α-Fe_2O_3/FCP could optimize the kinetics in water oxidation and improve the interfacial charge transfer for PEC water splitting. As a result, the optimal γ/α-Fe_2O_3/FCP composite photoanode exhibits the fast surface kinetics of

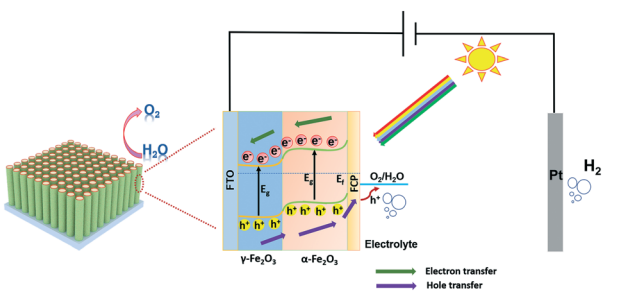

Scheme 1 The schematic band diagram illustrating the γ-Fe_2O_3/α-Fe_2O_3/FCP photoanode architecture with directions of charge separation and transportation.

α-Fe_2O_3 and a considerably negative onset potential, achieving a remarkable photocurrent density of up to 3.5 mA cm^{-2} at 1.23 V *vs.* RHE, which is 8.7 times higher than that of pure α-Fe_2O_3. The excellent bi-functional effects originate from the rapid interfacial hole injection and long-lived charge separation states (~50.64 ps) as investigated by fs-TAS, indicating that the core–shell nanorod structure loaded with FeCo Prussian blue (FCP) could boost the water oxidation kinetics and charge transfer efficiency. This work provides an effective insight into designing an outstanding water splitting photoanode.

Conflicts of interest

There are no conflicts to declare.

Acknowledgements

We are grateful to the National Natural Science Foundation of China (No. 21773086, 21872063).

Notes and references

1 D. Zhang, W. He, J. Ye, X. Gao, D. Wang and J. Song, *Small*, 2021, 2005149.
2 Y. Xu, Z. Zhang, C. Qiu, S. Chen, X. Ling and C. Su, *ChemSusChem*, 2021, **14**, 582–589.
3 X. Ren, Y. Ji, Y. Zhai, N. Yuan, J. Ding, Y. Li, J. Yan and S. F. Liu, *J. Energy Chem.*, 2021, **60**, 512–521.
4 W. Fu, X. Guan, Y. Si and M. Liu, *Chem. Eng. J.*, 2021, **410**, 128391.
5 S. Lin, H. Ren, Z. Wu, L. Sun, X.-G. Zhang, Y.-M. Lin, K. H. L. Zhang, C.-J. Lin, Z.-Q. Tian and J.-F. Li, *J. Energy Chem.*, 2021, **59**, 721–729.
6 H. Li, M. Yin, X. Li and R. Mo, *ChemSusChem*, 2021, 1–11.
7 Y. Fan, X. Ning, Q. Zhang, H. Zhao, J. Liu, P. Du and X. Lu, *ChemSusChem*, 2021, **14**, 1414–1422.
8 C. Li, T. Wang, Z. Luo, S. Liu and J. Gong, *Small*, 2016, **12**, 3415–3422.
9 T. H. Jeon, G.-h. Moon, H. Park and W. Choi, *Nano Energy*, 2017, **39**, 211–218.
10 F. Feng, C. Li, J. Jian, F. Li, Y. Xu, H. Wang and L. Jia, *J. Power Sources*, 2020, **449**, 227473.
11 T. Jiao, C. Lu, D. Zhang, K. Feng, S. Wang, Z. Kang and J. Zhong, *Appl. Catal., B*, 2020, **269**, 118768.
12 C. Li, Z. Luo, T. Wang and J. Gong, *Adv. Mater.*, 2018, **30**, e1707502.
13 H. Zhang, D. Li, W. J. Byun, X. Wang, T. J. Shin, H. Y. Jeong, H. Han, C. Li and J. S. Lee, *Nat. Commun.*, 2020, **11**, 4622.
14 M. Li, Y. Yang, Y. Ling, W. Qiu, F. Wang, T. Liu, Y. Song, X. Liu, P. Fang, Y. Tong and Y. Li, *Nano Lett.*, 2017, **17**, 2490–2495.
15 Y. L. Tong, B. Q. Chi, D. L. Qi and W. Zhang, *RSC Adv.*, 2021, **11**, 1233–1240.
16 R. Kant, S. Pathak and V. Dutta, *Sol. Energy Mater. Sol. Cells*, 2018, **178**, 38–45.
17 A. Helal, F. A. Harraz, A. A. Ismail, T. M. Sami and I. A. Ibrahim, *Appl. Catal., B*, 2017, **213**, 18–27.
18 P. I. Kyesmen, N. Nombona and M. Diale, *J. Alloys Compd.*, 2021, **863**, 158724.
19 Y. Makimizu, N. T. Nguyen, J. Tucek, H. J. Ahn, J. Yoo, M. Poornajar, I. Hwang, S. Kment and P. Schmuki, *Chemistry*, 2020, **26**, 2685–2692.
20 S. Zhang, P. Shangguan, S. Tong, Z. Zhang and W. Leng, *J. Phys. Chem. C*, 2019, **123**, 24352–24361.
21 Q. Bu, S. Li, Q. Wu, L. Bi, Y. Lin, D. Wang, X. Zou and T. Xie, *ChemSusChem*, 2018, **11**, 3486–3494.
22 Q. Bu, S. Li, K. Zhang, Y. Lin, D. Wang, X. Zou and T. Xie, *ACS Sustainable Chem. Eng.*, 2019, **7**, 10971–10978.
23 Z. Wang, J. Rong, J. Lv, R. Chong, L. Zhang, L. Wang, Z. Chang and X. Wang, *J. Energy Chem.*, 2021, **56**, 152–161.
24 S.-S. Yi, B.-R. Wulan, J.-M. Yan and Q. Jiang, *Adv. Funct. Mater.*, 2019, **29**, 1801902.
25 R. Shen, L. Zhang, X. Chen, M. Jaroniec, N. Li and X. Li, *Appl. Catal., B*, 2020, **266**, 118619.
26 Y. Li, Q. Wu, Q. Bu, K. Zhang, Y. Lin, D. Wang, X. Zou and T. Xie, *Chin. J. Catal.*, 2021, **42**, 762–771.
27 R. Zhang, L. Bi, D. Wang, Y. Lin, X. Zou and T. Xie, *Catal. Commun.*, 2020, **142**, 106028.
28 T.-F. Hou, M. A. Johar, R. Boppella, M. A. Hassan, S. J. Patil, S.-W. Ryu and D.-W. Lee, *J. Energy Chem.*, 2020, **49**, 262–274.
29 Y. Li, Z. Tang, J. Zhang and Z. Zhang, *Appl. Catal., B*, 2017, **207**, 207–217.
30 H. Zhang, L. Ma, J. Ming, B. Liu, Y. Zhao, Y. Hou, Z. Ding, C. Xu, Z. Zhang and J. Long, *Appl. Catal., B*, 2019, **243**, 481–489.
31 H. Sun, C. Neumann, T. Zhang, M. Loffler, A. Wolf, Y. Hou, A. Turchanin, J. Zhang and X. Feng, *Adv. Mater.*, 2019, **31**, e1900961.
32 J. H. Kim, J. H. Kim, J. H. Kim, Y. K. Kim and J. S. Lee, *Sol. RRL*, 2019, **4**, 1900328.
33 Q. Wu, Q. Bu, S. Li, Y. Lin, X. Zou, D. Wang and T. Xie, *J. Alloys Compd.*, 2019, **803**, 1105–1111.
34 D. Chen, Z. Liu and S. Zhang, *Appl. Catal., B*, 2020, **265**, 118580.
35 D. Cao, H. Li, L. Pan, J. Li, X. Wang, P. Jing, X. Cheng, W. Wang, J. Wang and Q. Liu, *Sci. Rep.*, 2016, **6**, 32360.
36 B. Moss, F. S. Hegner, S. Corby, S. Selim, L. Francàs, N. López, S. Giménez, J.-R. Galán-Mascarós and J. R. Durrant, *ACS Energy Lett.*, 2018, **4**, 337–342.
37 Y. Zhang, J. He, Q. Yang, H. Zhu, Q. Wang, Q. Xue and L. Yu, *J. Power Sources*, 2019, **440**, 227120.
38 C. Yang, J. Zhang, X. Zhu, Y. Liu, Y. Chen and C. Wang, *Appl. Surf. Sci.*, 2020, **529**, 147060.
39 H. Lan, A. Wei, H. Zheng, X. Sun and J. Zhong, *Nanoscale*, 2018, **10**, 7033–7039.
40 M. C. Biesinger, B. P. Payne, A. P. Grosvenor, L. W. M. Lau, A. R. Gerson and R. S. C. Smart, *Appl. Surf. Sci.*, 2011, **257**, 2717–2730.
41 J. L. Ortiz-Quinonez, U. Pal and M. S. Villanueva, *ACS Omega*, 2018, **3**, 14986–15001.
42 B. Sun, W. Zhou, H. Li, L. Ren, P. Qiao, F. Xiao, L. Wang, B. Jiang and H. Fu, *Appl. Catal., B*, 2018, **221**, 235–242.

43 K. Fan, H. Chen, B. He and J. Yu, *Chem. Eng. J.*, 2020, **392**, 123744.
44 S. Li, Q. Zhao, D. Meng, D. Wang and T. Xie, *J. Mater. Chem. A*, 2016, **4**, 16661–16669.
45 Y. Jin, L. Dang, H. Zhang, C. Song, Q. Lu and F. Gao, *Chem. Eng. J.*, 2017, **326**, 292–297.
46 A. Govind Rajan, J. M. P. Martirez and E. A. Carter, *ACS Catal.*, 2020, **10**, 11177–11234.
47 S. Cao, J. Low, J. Yu and M. Jaroniec, *Adv. Mater.*, 2015, **27**, 2150–2176.
48 B. Zhang, L. Chou and Y. Bi, *Appl. Catal., B*, 2020, **262**, 258–265.
49 C. Feng, Q. Zhou, B. Zheng, X. Cheng, Y. Zhang and Y. Bi, *J. Mater. Chem. A*, 2019, **7**, 22274–22278.
50 T. Jiang, T. Xie, W. Yang, L. Chen, H. Fan and D. Wang, *J. Phys. Chem. C*, 2013, **117**, 4619–4624.
51 T. Jiang, T. Xie, L. Chen, Z. Fu and D. Wang, *Nanoscale*, 2013, **5**, 2938–2944.
52 L. Bi, X. Gao, Z. Ma, L. Zhang, D. Wang and T. Xie, *ChemCatChem*, 2017, **9**, 3779–3785.
53 Y. Li, Q. Wu, K. Zhang, B. Hu, Y. Lin, D. Wang and T. Xie, *Chem. Res. Chin. Univ.*, 2020, **36**, 1059–1067.
54 W. Wang, Y. Tao, L. Du, Z. Wei, Z. Yan, W. K. Chan, Z. Lian, R. Zhu, D. L. Phillips and G. Li, *Appl. Catal., B*, 2021, **282**, 119568.
55 F. Liu, R. Shi, Z. Wang, Y. Weng, C. M. Che and Y. Chen, *Angew. Chem., Int. Ed.*, 2019, **58**, 11791–11795.
56 M. Sachs, J. S. Park, E. Pastor, A. Kafizas, A. A. Wilson, L. Francas, S. Gul, M. Ling, C. Blackman, J. Yano, A. Walsh and J. R. Durrant, *Chem. Sci.*, 2019, **10**, 5667–5677.
57 Y. Li, Q. Wu, Y. Chen, R. Zhang, C. Li, K. Zhang, M. Li, Y. Lin, D. Wang, X. Zou and T. Xie, *Appl. Catal., B*, 2021, **290**, 120058.

